Published paper

Mann, B.P. and Sims, N.D. (2009) *Energy harvesting from the nonlinear oscillations of magnetic levitation.* Journal of Sound and Vibration, 319 (1-2). pp. 515-530.

http://dx.doi.org/10.1016/j.jsv.2008.06.011

Energy Harvesting from the Nonlinear Oscillations of Magnetic Levitation

B.P. Mann

Dept. of Mechanical Engineering & Material Science, Duke University, Durham, NC, USA 27708

N.D. Sims

Dept. of Mechanical Engineering, Sheffield University, Sheffield, UK S1 3JD

Abstract

This paper investigates the design and analysis of a novel energy harvesting device that uses magnetic levitation to produce an oscillator with a tunable resonance. The governing equations for the mechanical and electrical domains are derived to show the designed system reduces to the form of a Duffing oscillator under both static and dynamic loads. Thus, nonlinear analyses are required to investigate the energy harvesting potential of this prototypical nonlinear system. Theoretical investigations are followed by a series of experimental tests that validate the response predictions. The motivating hypothesis for the current work was that nonlinear phenomenon could be exploited to improve the effectiveness of energy harvesting devices.

Key words: Energy harvesting, Duffing equation, nonlinear vibration, electromagnetic induction, magnetic levitation

PACS:

1 Introduction

The concept of vibration-based energy harvesting has received much attention in recent years. For example, several works have investigated the development of energy harvesters for low-power microelectromechanical systems or MEMS [1–3]. A particularly motivating circumstance is the development of wireless sensor networks that could be used in inaccessible or potentially hostile environments to transmit information in a wireless fashion. Most if not all of these works have focused on the power harvested when the response behavior can be adequately characterized as a linear oscillator with harmonic excitation. A resounding conclusion from the literature on energy harvesters operating within the linear regime is that the maximum power is generated when the system is excited at resonance. Thus, the prototypical approach is to design and fabricate energy harvesting devices so that the system's linear resonance matches the excitation frequency [1, 4–6]. This places an inconvenient constraint on the fabrication processes that are used to construct an energy harvester (i.e. consider MEMS resonators where the frequency of the mechanical resonance can be very sensitive to small dimensional imperfections).

The present paper explores an alternative approach by considering the energy harvesting potential when the nonlinearities of the system are sufficiently engaged. The motivating question is whether system nonlinearities can be used to improve the energy harvesting capability? For instance, the design-for-resonance approach places several performance limitations on the energy harvester. Specifically, a linear device is known to under perform when the system's resonance and excitation frequency do not coincide. Alternatively, the energy from multi-frequency and/or broad-band excitation may not be adequately captured. Problems also arise in application areas where the ex-

citation frequency varies since the linear harvester will underperform unless the complexity of the energy harvester is increased by adding more degrees of freedom (e.g. multiple oscillators [7,8]). While it is not the author's aim to address whether a single system or approach can be used to resolve all of the aforementioned complications, we would simply like to draw attention to the fact that alternative strategies are needed to expand the range of possibilities that designers can implement for improved energy extraction.

A variety of methods have been used to convert environmental energy into electric energy [3]. For instance, capacitive energy harvesters with either a bias voltage or electret charge have been described in references [3, 9]. Another approach is to use piezoelectric materials to convert mechanical strain into electrical energy. For instance, several authors have investigated piezoelectric devices that harvest energy from impact, vibration, and acoustic sources [5,10–12]. Induction is a third approach that may be used to convert environmental energy into electrical energy. Some recent work in this area includes the investigation of a single translating magnet generator and rotating microgenerators [13, 14].

This paper describes the design and analysis of a novel energy harvesting device that uses magnetic forces to levitate an oscillating center magnet. A specific goal was to use the nonlinear restoring forces to enable tuning of the system's linear resonance - thus alleviating the need to precisely fabricate the device. The formulation of the system's governing equations shows the device can be modeled with Duffing's equation under static and harmonic excitation. Investigating the frequency response for this nonlinear system reveals the fact that engaging the system's nonlinear response could improve the energy harvested.

The work of this paper is organized as follows. The next section describes the experimental system, the governing equations, and the use of the magnetic restoring forces to tune the system's linear resonance. The third section examines the frequency response of the system under harmonic base excitation, contrasts the response of the current system to a linear counterpart, and investigates the trends related to changes in the electrical load. This is followed by a series of detailed experiments that compare the theoretical predictions with experimental measurements. The final section describes the salient features of this work and describes some final remarks.

2 Experimental apparatus

This section describes the calibration of a restoring force model that is used to predict the system's linear resonance under small changes in the magnet spacing. In addition, a model is presented for the interaction of mechanical and electrical components which allows the governing equations to be reduced to the form of Duffing's equation.

2.1 Magnetic levitation and restoring forces

A schematic diagram of the magnetic levitation system is shown in Fig. 1. The device used two outer magnets that were mechanically attached to a threaded support. The threaded supports were inserted into the ends of a teflon tube and used to vary the spacing between the magnets. A center magnet was placed between the two outer magnets and the magnetic poles were oriented to repel the center magnet - thus suspending the center magnet with a nonlinear restoring force. Here, we emphasize a paradigm shift by noting that

nonlinearity is an integral feature of the energy harvester design. In particular, it will be shown that nonlinearity allows the linear resonance to be tuned by simply changing the spacing between the upper and lower magnets.

Magnetic restoring forces were calibrated from measurements of the restoring force and separation distance between the bottom and center magnet. Figure 1b shows a series of experimental measurements plotted as a function of the separation distance between two magnets. These measurements were fitted to a power series

$$F_s(s) = \sum_{n=0}^{3} \alpha_n s^n \,, \tag{1}$$

where s is the separation distance and the coefficients α_0-α_3 are obtained using a least-squares procedure. The quality of the fitted coefficients was verified from an overlay of the experimental measurements onto the power series (see Fig. 1b). Force-displacement relationships were then formulated by writing the separation distance as a function of the center magnet displacement, x. The force-displacement relationships for the top, $F_t(x)$, and bottom magnets, $F_b(x)$, are

$$F_b(x) = \sum_{n=0}^{3} \alpha_n \left(x + d_o\right)^n \,, \tag{2a}$$

$$F_t(x) = \sum_{n=0}^{3} \alpha_n \left(d_o - x\right)^n \,, \tag{2b}$$

where d_o is the spacing between the magnets shown in Fig. 1a. The total restoring force is given by a vector summation of the restoring forces acting on the top and bottom magnets, $F(x) = F_b(x) - F_t(x)$,

$$F(x) = \left(2\alpha_1 + 4d_o\alpha_2 + 6d_o^2\alpha_3\right) x + 2\alpha_3 x^3 = kx + k_3 x^3\,, \tag{3}$$

where $k = 2\alpha_1 + 4d_o\alpha_2 + 6d_o^2\alpha_3$ is the linear stiffness coefficient and $k_3 = 2\alpha_3$. Figure 2a shows the force-displacement relationship for the estimated parameters when $d_o = 37.3$ (mm) for the experimentally identified parameters $\alpha_1 = 36.04$ (N/m), $\alpha_2 = -4.12 \times 10^3$ (N/m^2), and $\alpha_3 = 6.92 \times 10^4$ (N/m^3). An inspection of Eq. (3), will lead to two important conclusions: 1) changes in the magnet spacing, d_o, will alter the linear stiffness and resonance; and 2) the nonlinear term is independent of d_o (at the current approximation level), thus changes in magnet spacing will alter the importance of the nonlinearity by increasing/decreasing the influence of the linear stiffness.

2.2 Tuning linear resonance

This section describes a potentially beneficial feature of nonlinearity in the restoring force. Specifically, the nonlinear restoring forces can enable the linear resonance to be tuned for changes in static displacement. An expression for the linear resonance can be developed from the governing equation for undamped and unforced oscillations,

$$m\ddot{x} + kx + k_3 x^3 = -mg\,, \tag{4}$$

where $m = 19.5$ (g) is the magnet mass and $g = 9.81$ (m/s^2) is the gravitational constant. Static equilibrium, x_e, is found by equating the time-varying terms of Eq. (4) to zero to obtain

$$x_e^3 + \frac{k}{k_3} x_e + \frac{mg}{k_3} = 0\,. \tag{5}$$

The undamped oscillations about the nonlinear equilibrium position are found by substituting $x = x_e + \xi(t)$ into Eq. (4). Dividing by the mass, the coefficient of the linear term becomes the linear resonance. Here, the resonance is expressed in terms of both the series expansion coefficients and the restoring force coefficients

$$\omega_n^2 = \frac{2\alpha_1 + 4\alpha_2 d_o + 6\alpha_3 \left(d_o^2 + x_e^2\right)}{m} = \frac{1}{m}\left(k + 3k_3 x_e^2\right)\,. \tag{6}$$

Figure 2 shows a plot of the linear resonance for changes in the outer magnet spacing. Here, it is interesting to note that the resonance approximately follows a linear tuning relationship until it reaches a final threshold.

2.3 Governing equations and energy harvesting model

A schematic diagram of the complete energy harvesting device is shown in Fig. 3. The device consists of the previously mentioned magnetic levitation system and a coil fabricated from seven layers of 36 guage enamel-coated copper wire that was wound around the outer casing. To describe the model for electromagnetic induction, we refer to the schematic diagram of Fig. 3b where two reference frames have been applied. The first reference frame is fixed in space and is used to describe the motion amplitude, A, and excitation frequency, Ω, of the outer housing $z = A\cos\Omega t$. The second reference frame, designated as x, describes the motion of the center magnet. In agreement with the work of reference [1], the coil magnetic force is assumed to be proportional

to the relative velocity between the center magnet and outer housing.

The equation for the electrical circuit is obtained by applying Kirchoff's law to the electrical circuit of Fig. 3a,

$$i\,(R_{load} + R_{int}) - \alpha\,(\dot{x} - \dot{z}) = 0\,, \tag{7}$$

where i is the electrical current, R_{int} is the internal resistance of the coil, R_{load} is the resistance of the external load, and α is the electromechanical coupling coefficient. This term is commonly expressed as $\alpha = NBl$ where N is the number of coil turns, B is the average magnetic field strength, and l is the coil length. The following governing equation for the mechanical system is obtained from a summation of forces in the vertical direction

$$m\ddot{x} + c_m(\dot{x} - \dot{z}) + k(x - z) + k_3(x - z)^3 + \alpha i = -mg\,, \tag{8}$$

where c_m is the damping coefficient used to described the mechanical damping. This is introduced to approximate the energy losses from viscous damping and friction. An expression for the electrical damping coefficient is obtained by solving Eq. (7) for the current,

$$i = \alpha \frac{\dot{x} - \dot{z}}{R_{load} + R_{int}}\,, \tag{9}$$

where the current leads to a force that opposes the relative motion due to Lenz's law [15]. Specifically, electrical damping arises due the introduction of a coil to convert the vibration energy into electrical energy. The expression for the electrical damping coefficient is $c_e = \alpha^2/(R_{load} + R_{int})$. Equation (9) can

be substituted into Eq. (8) to obtain a revised governing equation

$$m\ddot{x} + c(\dot{x} - \dot{z}) + k(x - z) + k_3(x - z)^3 = -mg\,. \tag{10}$$

where $c = c_m + c_e$ is the damping coefficient used to described the combined mechanical and electric damping. In the next section, the model of Eq. (10) is examined to determine the relative velocity, output voltage, and system power.

3 Analysis of harmonic base excitation

This section investigates the nonlinear response and energy harvesting potential of the system. A change in variable, $y = x - z$, is substituted into Eq. (10) to obtain a governing equation written in terms of the relative displacement between the center magnet and outer housing

$$\ddot{y} + 2\zeta\omega\dot{y} + \omega^2 y + \beta y^3 = F_o + F_1 \cos\Omega t\,, \tag{11}$$

where the coefficients of Eq. (10) have been rewritten as

$$2\zeta\omega = \frac{c}{m}\,, \tag{12a}$$

$$\omega^2 = \frac{k}{m}\,, \tag{12b}$$

$$\beta = \frac{k_3}{m}\,, \tag{12c}$$

$$F_o = g\,, \tag{12d}$$

$$F_1 = \Omega^2 A\,, \tag{12e}$$

Next, several terms from Eq. (11) are reordered to aid in the nonlinear analysis that follows,

$$\ddot{y} + 2\epsilon\mu\dot{y} + \omega^2 y + \epsilon\hat{\beta}y^3 = F_o + 2\epsilon\hat{F}_1 \cos\Omega t\,, \tag{13}$$

where ϵ has been introduced as a book keeping parameter and the terms $2\epsilon\mu = 2\zeta\omega$, $\epsilon\hat{\beta} = \beta$, and $2\epsilon\hat{F}_1 = F_1$ have been applied. The goal of the next section is to analyze Eq. (13) to obtain an expression for the response amplitude of the system under harmonic base excitation.

3.1 Frequency response from the Method of Multiple Scales

This section derives the frequency response of the system using a perturbation technique known as multiple scales. While many researchers have applied this approach to nonlinear oscillation problems [16], we show the derivation of the frequency response for the sake of completeness. The assumed solution to Eq. (13) is written as a first order expansion

$$y(\tau, \epsilon) = y_0(\tau, \tau_1) + \epsilon y_1(\tau, \tau_1)\,, \tag{14}$$

where the independent time scales are defined as $\tau = t$, $\tau_1 = \epsilon\tau$. It follows that the derivatives with respect to time become partial derivatives with respect to the corresponding time scale

$$\frac{d}{dt} = \frac{\partial}{\partial \tau} + \frac{d\tau_1}{d\tau}\frac{\partial}{\partial \tau_1} = D_0 + \epsilon D_1 \,, \tag{15a}$$

$$\frac{d^2}{dt^2} = D_0^2 + 2\epsilon D_0 D_1 \,. \tag{15b}$$

Substituting Eqs. (14)–(15b) into Eq. (13) and separating the result into the orders of epsilon $\mathcal{O}(\epsilon)$ gives the following two linear equations

$$\mathcal{O}(\epsilon^0) : D_0^2 y_0 + \omega^2 y_0 = F_o \,, \tag{16a}$$

$$\mathcal{O}(\epsilon^1) : D_0^2 y_1 + \omega^2 y_1 = -2D_0 D_1 y_0 - 2\mu D_0 y_0 - \hat{\beta} y_0^3 + 2\hat{F}_1 \cos\Omega t \,, \tag{16b}$$

where the terms of $\mathcal{O}(\epsilon^2)$ and higher have been neglected - as in the expansion defined by Eq. (14). The solution to the $\mathcal{O}(\epsilon^0)$ equation is of the form

$$y_0 = A(\tau_1)e^{i\omega\tau} + \bar{A}(\tau_1)e^{-i\omega\tau} + \frac{F_o}{\omega^2} \,, \tag{17}$$

where $A(\tau_1)$ and $\bar{A}(\tau_1)$ are complex conjugates that are functions of the higher time scale. This solution is substituted into the $\mathcal{O}(\epsilon^1)$ equation to obtain

$$\begin{aligned} D_0^2 y_1 + \omega^2 y_1 = -2i\omega\Big[A(\tau_1)' + \mu A(\tau_1)\Big]e^{i\omega\tau} - \hat{\beta}\Big[3A^2(\tau_1)\bar{A}(\tau_1) + \frac{3A(\tau_1)F_o^2}{\omega^4}\Big]e^{i\omega\tau} \\ - \hat{\beta}\left[A(\tau_1)^3 e^{3i\omega\tau} + \frac{3F_o}{\omega^2}A^2(\tau_1)\bar{A}(\tau_1)e^{2i\omega\tau} + \frac{F_o}{\omega^2}\left(3A(\tau_1)\bar{A}(\tau_1) + \frac{F_o^2}{2\omega^4}\right)\right] \\ + 2\hat{F}_1\cos\Omega t + CC \,, \end{aligned} \tag{18}$$

where the prime denotes a derivate with respect to τ_1 and CC denotes the complex conjugates of the terms on the right hand side. A choice must now be

made on whether a more accurate solution is preferred for the near or away from resonance. Since it is common to excite the system close to resonance, we have chosen to obtain a more accurate frequency response near resonance. Thus, near resonance excitation is assumed and the following substitution, $\Omega = \omega + \epsilon\sigma$, is introduced into Eq. (18) to describe the nearness of Ω to ω. The term σ is often called a detuning parameter and acts to describe the nearness of Ω to ω. The $\mathcal{O}(\epsilon^1)$ equation after substitution becomes

$$D_0^2 y_1 + \omega^2 y_1 = -2i\omega\Big[A(\tau_1)' + \mu A(\tau_1)\Big]e^{i\omega\tau} - \hat{\beta}\Big[3A^2(\tau_1)\bar{A}(\tau_1) + \frac{3A(\tau_1)F_o^2}{\omega^4}\Big]e^{i\omega\tau} - \hat{\beta}\left[A(\tau_1)^3 e^{3i\omega\tau} + \frac{3F_o}{\omega^2}A^2(\tau_1)\bar{A}(\tau_1)e^{2i\omega\tau} + \frac{F_o}{\omega^2}\left(3A(\tau_1)\bar{A}(\tau_1) + \frac{F_o^2}{2\omega^4}\right)\right] + \hat{F}_1 e^{i(\omega\tau+\sigma\tau_1)} + CC\,, \quad (19)$$

The next step requires eliminating the terms in Eq. (18) that cause an unbounded solution. These terms, the coefficients that multiply $e^{i\omega\tau}$ in Eq. (19), are commonly referred to as secular terms. They are eliminated by setting them to equal zero

$$-2i\omega\Big(A(\tau_1)' + \mu A(\tau_1)\Big) - 3\hat{\beta}\left(A^2(\tau_1)\bar{A}(\tau_1) + \frac{F_o^2}{\omega^4}A(\tau_1)\right) + \hat{F}_1 e^{\sigma\tau_1} = 0\,. \quad (20)$$

Following reference [17], the polar form $A(\tau_1) = \frac{1}{2}a(\tau_1)e^{i\phi(\tau_1)}$ is now introduced into the above equation. After simplifying the result, the following equation is obtained

$$-i\omega\Big(a' + ai\phi' + \mu a\Big) - \frac{3}{8}\hat{\beta}\left(a^3 + 4a\frac{F_o^2}{\omega^4}\right) + \hat{F}_1 e^{i(\sigma\tau_1-\phi)} = 0\,, \quad (21)$$

Equation (21) is then separated into real and imaginary components. After the substitution of $\gamma = \sigma\tau_1 - \phi$, the resulting equations become

$$a\gamma' = a\sigma - \frac{3\hat{\beta}}{8\omega}\left(a^3 + 4a\frac{F_o^2}{\omega^4}\right) + \frac{\hat{F}_1}{\omega}\cos\gamma\,, \tag{22a}$$

$$a' = -\mu a + \frac{\hat{F}_1}{\omega}\sin\gamma\,. \tag{22b}$$

The equilibria solutions of Eq. (22a) and Eq. (22b) represent the steady-state periodic solutions of the system. They can be found by setting $\gamma' = 0$ and $a' = 0$. Squaring and adding these relationships results in an expression for the frequency response for the nonlinear system

$$\left[\mu^2 + \left(\sigma - \frac{3\hat{\beta}}{8\omega}\left(a^2 + 4\frac{F_o^2}{\omega^4}\right)\right)^2\right] a^2 = \frac{\hat{F}_1}{\omega^2}^2\,. \tag{23}$$

Before examining the response of the system, we expand Eq. (23) and rewrite it in terms of the physical parameters of the system. The modified frequency response equation is

$$\begin{aligned}\left(\frac{3\beta}{8\omega}\right)^2 a^6 + \left(\frac{9\beta^2 F_o^2}{8\omega^6} + \frac{3}{4}\beta\left(1 - \frac{\Omega}{\omega}\right)\right) a^4 \\ + \left(\left(\frac{3\beta F_o^2}{2\omega^5}\right)^2 + \frac{3\beta F_o^2}{\omega^4}\left(1 - \frac{\Omega}{\omega}\right) + (\Omega - \omega)^2 + (\zeta\omega)^2\right) a^2 - \left(\frac{F_1}{2\omega}\right)^2 = 0\,.\end{aligned} \tag{24}$$

Although the above equation gives the response amplitude for the relative displacement, the relative velocity is the more meaningful quantity for the energy harvesting device. Thus the relative displacement response $y = a\cos(\Omega t - \gamma)$

must be differentiated to obtain the predicted relative velocity $\dot{y} = -\Omega a \cos(\Omega t - \gamma)$. In the results that follow, we report the absolute value of the relative velocity using the notation $|\dot{y}|$.

3.2 Example response predictions

The level of damping in the energy harvester can be modified by increasing or decreasing the resistance of the electrical load. To illustrate the energy harvesting considerations, a series of relative velocity predictions have been presented in Fig. 4 and Fig. 5. While each figure shows the relative velocity response for three different excitation levels, the damping level was increased for the results of Fig. 5 - representative of a decrease in the resistive load. One noticeable change is the significant decrease in the relative velocity that is associated with an increase in damping. In addition, the increased damping has alleviated the multiple periodic attractors and jump phenomena from the response of Fig. 5(b).

An interesting result from Fig. 4b and Fig. 4c is the extended range of large amplitude responses that are provided by engaging the nonlinearity of the system. In essence, these examples show the system nonlinearity could potentially be used to provide large relatively velocities over a wider range of excitation frequencies. Another important consideration is that the maximum relative velocity for Fig. 4b and Fig. 4c do not occur at the location of the linear resonance (i.e. results can be compared with those of Fig. 4a). The implications of this observation will be discussed further in the sections that follow.

3.3 Power delivered to the electrical circuit

Since the power transferred to the electrical domain is of primary importance, this section derives expressions for the power transferred to the electrical load. We have assumed that the system's response is dominated by a single harmonic in the results that follow. Using Eq. (7) or the results of reference [1], the current passing through the electrical load can be written as

$$i(t) = -\left(\frac{\alpha}{R_{load} + R_{int}}\right) \Omega a \sin(\Omega t - \gamma)\,. \tag{25}$$

The instantaneous power can then be computed from

$$P(t) = i^2 R_{load} = \frac{1}{2}\left(\frac{\alpha a \Omega}{R_{load} + R_{int}}\right)^2 R_{load}\left(1 - \cos 2(\Omega t - \gamma)\right)\,. \tag{26}$$

The average of Eq. (26) over a single period gives the following expression for the average power delivered to the electrical load

$$P_{av} = \left(\frac{\alpha a \Omega}{R_{load} + R_{int}}\right)^2 R_{load}\,. \tag{27}$$

Perhaps the most important quantity is the maximum average power that is delivered to the electrical load. This quantity is given by

$$P_{avmax} = \left(\frac{\alpha \Omega_{max} a_{max}}{(R_{load} + R_{int})}\right)^2 R_{load}\,, \tag{28}$$

where a_{max} is the maximum amplitude of the frequency response which occurs when the system is excited at $\Omega = \Omega_{max}$. Since the largest amplitude will occur away from the linear resonance, analytically computing P_{avmax} requires

further analysis. To compute the frequency of maximum response, Eq. (24) was differentiated with respect to both Ω and a. Next, the quantity differentiated with respect to a is inverted and multiplied by the quantity that was differentiated with respect to Ω to obtain $da/d\Omega$. After setting $da/d\Omega = 0$, the following relationships was obtained to relate a_{max} and Ω_{max},

$$\Omega_{max} = \frac{3\beta}{8\omega} a_{max}^2 + \frac{3\beta F_o^2}{2\omega^5} + \omega \,. \tag{29}$$

An expression for the magnitude of the maximum response was obtained by substituting $\Omega = \Omega_{max}$ into Eq. (24) to obtain $a_{max} = \frac{F_1}{2\zeta\omega^2}$. After substituting this relationship into Eq. (29), the excitation frequency where the maximum response occurs can be found

$$\Omega_{max} = \frac{3\beta F_1^2}{32\omega^5\zeta^2} + \frac{3\beta F_o^2}{2\omega^5} + \omega \,. \tag{30}$$

Substituting Eq. (30) into Eq. (28) then gives the final expression for the maximum power in terms of the system parameters and the excitation amplitude

$$P_{avmax} = \left(\alpha F_1 \frac{3F_1^2\beta + 48\beta F_o^2\zeta^2 + 32\zeta^2\omega^2}{64\zeta^3\omega^7(R_{int} + R_{load})} \right)^2 R_{load} \,. \tag{31}$$

In the above expression, we note that F_1 is also a function of the excitation frequency since the base excitation was defined in terms of a constant displacement. However, writing Eq. (31) as shown is consistent with the experiments that follow where a constant seismic acceleration amplitude, F_1, was used for base excitation. We would also like to draw attention to the fact that the above expression is the exact solution for the derived frequency response. However, the authors recognize that the derived frequency response equation is not ex-

act. Furthermore, the response of the nonlinear system may also include sub- or super-harmonics which could potentially alter the derived relationship.

3.4 Comparison of linear and nonlinear energy harvesting

The past section highlights that the power delivered to the electrical load is proportional to the oscillator velocity amplitude. Thus the results of this paper will compare the relative velocity responses while recognizing that the power scales according to the results of Section 3.3. This section compares the relative velocity responses of the nonlinear device with those of a linear device. To define an equivalent linear oscillator, the linear system was assumed to be governed by

$$\ddot{y} + 2\gamma\omega_n\dot{y} + \omega_n^2 y = F_1 \cos\Omega t \tag{32}$$

where γ and ω_n are the damping ratio and natural frequency, respectively. Response comparisons were made by first establishing a baseline case which is shown in Fig. 6a. While the linear oscillator natural frequency was determined from the procedure outlined in Section 2.2, the damping ratio was set by matching the peak responses of the two systems in Fig. 6a.

One observation is that the response for both systems scales almost linearly within some regime of excitation amplitudes. However, once the nonlinearities have been sufficiently engaged, as shown in Fig. 6b and Fig. 6c, the peak response of the nonlinear system no longer scales linearly and is relocated away from linear resonance. Thus the ability to tune the restoring forces becomes an essential consideration for applications with a fixed-frequency harmonic

excitation. Another interesting aspect of the frequency response for the nonlinear system is the relatively large amplitudes that persist over a much larger range of frequencies. Certainly, this type of response could prove beneficial for applications with either fixed or varying excitation inputs.

Although the nonlinear response could be used for improved energy reclamation, multiple period solutions can also exists in some regions of the frequency response - one solution representing a relatively small response and the other representing the higher amplitude response. Since this region is sensitive to initial conditions, we note that a jump from the smaller response to the larger response could be triggered by a perturbation (i.e. from the basin of attraction of a small response to the basin of attraction for the larger response). For the present system, the perturbation could either be applied mechanically or electrically by momentarily increasing the coil current.

4 Experimental investigation

This section describes the series of experimental tests that were performed to compare experimental measurements with theoretical predictions. The experimental tests can be broadly separated into the performance of: 1) frequency sweeps or changes in the excitation frequency while holding all other experimental variables constant; and 2) excitation amplitude sweeps where the excitation amplitude was varied while holding the excitation frequency and all other variables constant. In an effort to capture hysteresis in the response behavior, along with the presence of multiple periodic attractors, both increasing and decreasing frequency and amplitude sweeps were performed.

4.1 Measurement and instrumentation

Figure 7 shows the primary equipment used during the experimental tests. Harmonic base excitation was applied by mounting the energy harvesting device to a LDS V400 modal shaker. To alleviate magnetic field interference from the shaker, an aluminum extension piece was used to distance the energy harvesting device away from the shaker base. Measurements of the shaker acceleration were obtained by mounting an accelerometer to the shaker mounting surface. When frequency sweeps were performed, it became necessary to control the shaker acceleration. Thus a shaker controller was used to monitor and control the amplitude of the shaker acceleration at the excitation frequency. Measurements of center magnet absolute velocity were obtained by shining a laser vibrometer through an access hole drilled in the top threaded support of the energy harvesting device (see Fig. 7).

Since the theoretical predictions focus on the relative motion between the center magnet and the outer housing, a series of calibration experiments were performed to relate measured coil voltages to the relative velocity. Furthermore, determining this calibration curve was required to compare theoretical predictions with experimental measurements. To make accurate predictions for the response of the system, the system damping was also required. The electrical damping was determined from the measured coil internal resistance $R_{int} = 188$ (Ohms), the resistance of the electrical load $R_{load} = 1\times10^6$ (Ohms), and the coil electromechanical coupling coefficient $\alpha = 7.752$ (volt·s/m). The total damping was then determined by combining the electrical damping, $c_e = 6.01 \times 10^{-5}$ (Ns/m), with the mechanical damping, $c_m = 0.190$ (Ns/m), to obtain the damping ratio reported in Table 1.

4.2 Comparisons of experiment with theory

The theoretical predictions of this section use the experimentally identified parameters of Table 1. The first series of experimental tests are shown in Fig. 8. This figure compares the response behavior from approximately 100 upward frequency sweeps, where the excitation was started at a low frequency and slowly increased, to the response behavior of 100 downward frequency sweeps, where the excitation frequency was started at a higher value and slowly decreased. In addition, theoretical velocity predictions are compared with the experimentally obtained velocity predictions. As shown in Fig. 8a, at relatively low excitation levels, the frequency response of the system look very similar to the response of a linear system (i.e. no hysteresis in upward or downward responses and only a single periodic attractor at each excitation frequency). However, the results of Fig. 8b show an increase in excitation amplitude will cause the appearance of multiple periodic attractors and hysteresis in the frequency response curves. Perhaps another interesting observation is that the measured experimental behavior compares favorably well with theoretical predictions. In particular, both theory and experiment capture the jump phenomena near the primary resonance and the presence of multiple periodic attractors under relatively large excitation amplitudes.

Another series of experimental tests are shown in Fig. 9. Here, the top graph shows the largest excitation amplitude used for the upward and downward frequency sweep tests. In graph (b), we show the results of experimental amplitude sweep tests. While approximately 100 responses were recorded for the upward and downward sweep test of Fig. 9a, relatively fewer results were recorded for the experiments of Fig. 9b. This is because the amplitude sweep results were obtain by manually increasing or decreasing the excitation am-

plitude. As in the results of the previous figure, experimental responses are found to compare favorably with theoretical predictions. However, both cases of Fig. 9 are shown to exhibit the jump phenomena.

5 Discussion

This paper describes the design and analysis of a novel energy harvesting device that uses magnetic restoring forces to levitate an oscillating center magnet. The mathematical model for the energy harvesting device is derived and then examined for the case of harmonic base excitation. Perhaps an interesting aspect is that the governing equation for relative displacement reduces to the form of Duffing's equation. The present investigations reveal that engaging the nonlinear response of system can result in relatively large oscillations over a wider range of frequencies - thus potentially improving the ability to harvest energy under certain circumstances.

Expressions that consider the coupling between the mechanical and electrical domains are derived for the for the instantaneous, maximum, and average power. Unlike energy harvesting devices that operate within a linear regime, the excitation frequency where the maximum power is delivered to the electrical load can be at a frequency away from linear resonance. Thus we have developed an expression for the excitation frequency where maximum power occurs.

The nonlinear response behavior of the harvester is shown to be strongly dependent on the damping level. Although we have derived expressions for the interplay between the parameters of the mechanical system and the electrically induced damping, we have not explicitly explored the maximum power

output for our experimental system. This was omitted because we recognized that an excessive level of input excitation would have been required to engage the nonlinear behavior - due to the relatively large mechanical damping. However, some practical improvements to the presented design, such as the implementation of methods to reduced the damping due to frictional contact between surfaces, could be implemented to reduce the mechanical damping.

The coexisting periodic solutions provide an additional complication that is not observed in the linear counterpart. Specifically, both low and a high-energy responses can coexists for the same parameter combinations. However, we suggest that one could use the coupling between the electrical circuit and mechanical oscillations to trigger a jump to the more desirable attractor. The developed theoretical studies are compared with a series of experimental tests to confirm the response behavior of the experimental system. As was noted previously, the response behavior of the experimental system is shown to compare favorably with theoretical predictions.

Acknowledgements

Mann acknowledges support from U.S National Science Foundation CAREER Award (CMS-0636641). Sims would like to acknowledge support from EPSRC (GR/S49841/01).

References

[1] N. G. Stephen, On energy harvesting from ambient vibration, Journal of Sound and Vibration 293 (2006) 409–425.

[2] S. P. Beeby, M. J. Tudor, N. M. White, Energy harvesting vibration sources for microsystems applications, Measurement Science and Technology 17 (2006) 175–195.

[3] S. Roundy, P. K. Wright, J. M. Rabaey, Energy Scavenging for Wireless Sensor Networks, Springer-Verlag, New York, 2003.

[4] G. A. Lesieutre, G. K. Ottman, H. F. Hofmann, Damping as a result of piezoelectric energy harvesting, Journal of Sound and Vibration 269 (3-5) (2004) 991 – 1001.

[5] H. A. Sodano, D. J. Inman, G. Park, Generation and storage of electricity from power harvesting devices, Journal of Intelligent Material Systems and Structures 16 (2005) 67–75.

[6] H. A. Sodano, D. J. Inman, G. Park, Comparison of piezoelectric energy harvesting devices for recharging batteries, Journal of Intelligent Material Systems and Structures 16 (2005) 799–807.

[7] S. M. Shahruz, Design of mechanical band-pass filters for energy scavenging, Journal of Sound and Vibration 292 (3-5) (2006) 987–998.

[8] S. M. Shahruz, Limits of performance of mechanical band-pass filters used in energy scavenging, Journal of Sound and Vibration 293 (1-2) (2006) 449–461.

[9] B. C. Yen, J. H. Lang, A variable-capacitance vibration-to-electric energy harvester, IEEE Transactions on Circuits and Systems 1 –Fundamental Theory and Applications 53 (2) (2005) 288 –295.

[10] M. Umeda, K. Nakamura, S. Ueha, Energy storage characteristics of piezo-generator using impact induced vibrations, Japan Journal of Applied Physics 36 (1997) 3146–3151.

[11] J. H. Cho, R. F. Richards, D. F. Bahr, C. D. Richards, Efficiency of energy conversion by piezoelectrics, Applied Physics Letters 89 (2006) 104107.

[12] S. B. Horowitz, M. Sheplak, L. N. Cattafesta, T. Nishida, A mems acoustic energy harvester, Journal Micromechanics and Microengineering 16 (2006) 174–181.

[13] C. B. Williams, R. B. Yates, Analysis of a microgenerator for microsystems, in: Proceedings of the 8th International Conference on Solid-State Sensors and Actuators, Stockholm, Sweden, Eurosensors IX, 1995, pp. 87–B4.

[14] D. P. Arnold, F. Herrault, I. Zana, P. Galle, J. par, S. Das, J. H. Lang, M. G. Allen, Design optimization of an 8-watt, microscale, axial-flux, permanent-magnet generator, Journal of Micromechanics and Microengineering 9 (2006) 290–296.

[15] D. Haliday, R. Resnick, Fundamentals of Physics, 3rd Edition, John Wiley & Sons, Inc., New York, NY, 1988.

[16] A. H. Nayfeh, D. T. Mook, Nonlinear Oscillations, John Wiley & Sons, Inc., New York, 1979.

[17] A. H. Nayfeh, B. Balachandran, Applied Nonlinear Dynamics, 1st Edition, John Wiley & Sons, Inc., New York, NY, 1995.

Table 1

Identified model parameters for the experimental system that were applied during theoretical studies. Reported relationships are for $d_o = 36.3$ (mm).

Parameter	Value	Units
m	0.0195	Kg
k	35.0	N/m
k_3	1.384×10^5	$\mathrm{N/m^3}$
ω	42.36	rad/s
ζ	0.115	none
β	7.098×10^6	$\mathrm{N/Kg\ m^3}$
F_o	-9.81	$\mathrm{m/s^2}$

Fig. 1. A schematic diagram of the magnetic levitation system with threaded supports to position the outer magnets is shown in (a). Graph (b) shows the restoring force plotted as a function of the separation distance between the center and bottom magnet.

Fig. 2. Graph (a) shows the force-displacment relationship for $d_o = 37.3$ (mm) and the coefficients of Table 1. Graph (b) illustrates a change in the linear resonances as a function of the magnet spacing.

Fig. 3. Circuit diagram (a) for the energy harvesting device shown in (b).

Fig. 4. Relative velocity response for different excitation amplitudes: (a) $F_1 = 0.1$ (m/s^2), (b) $F_1 = 2$ (m/s^2), and (c) $F_1 = 4$ (m/s^2). With the exception of the damping ratio, set to $\zeta = 0.05$, the experimentally identified parameters from Table 1 were used. Solid line denotes stable periodic solutions and a dashed line represents unstable periodic solutions.

Fig. 5. Relative velocity response for different excitation amplitudes: (a) $F_1 = 0.1$ (m/s^2), (b) $F_1 = 2$ (m/s^2), and (c) $F_1 = 4$ (m/s^2). With the exception of the damping ratio, set to $\zeta = 0.09$, the experimentally identified parameters from Table 1 were used. Solid line denotes stable periodic solutions and a dashed line represents unstable periodic solutions.

Fig. 6. Frequency response curves of the relative velocity for the magnetic levitation system and a linear oscillator with parameters $\gamma = 0.036$ and $\omega_n = 49.87$ (rad/s) which give matching peak responses for $F_1 = 0.1$ (m/s^2), graph (a). The remaining graphs are for relatively larger excitation amplitudes: (b) $F_1 = 2$ (m/s^2) and (c) $F_1 = 4$ (m/s^2). Solid line denotes stable periodic solutions and a dashed line represents unstable periodic solutions.

Fig. 7. Schematic diagram of the primary experimental instrumentation and shaker controller. A laser vibrometer was used to measure the absolute velocity of the center magnet during calibration. Afterwards, the center magnet velocity was determined from the measured coil voltage.

Fig. 8. Experimental velocity response amplitudes from forward (red dots) and reverse frequency sweeps (green circles) are compared with theory. Theoretical predictions are separated into stable solutions (solid black line) and unstable solutions (dashed black line). Graph (a) shows results for $F_1 = 2.1$ (m/s^2) and the results of graph (b) are for $F_1 = 8.4$ (m/s^2).

Fig. 9. Experimental velocity response amplitudes from forward (red dots) and reverse frequency sweeps (green circles) are compared in graph (a) for $F_1 = 9.3$ (m/s^2). Graph (b) shows velocity response amplitudes results from upward and downward input excitation amplitude sweeps for a constant frequency of $\Omega = 20.8\pi$ (rad/s). Theoretical predictions are separated into stable solutions (solid black line) and unstable solutions (dashed black line).

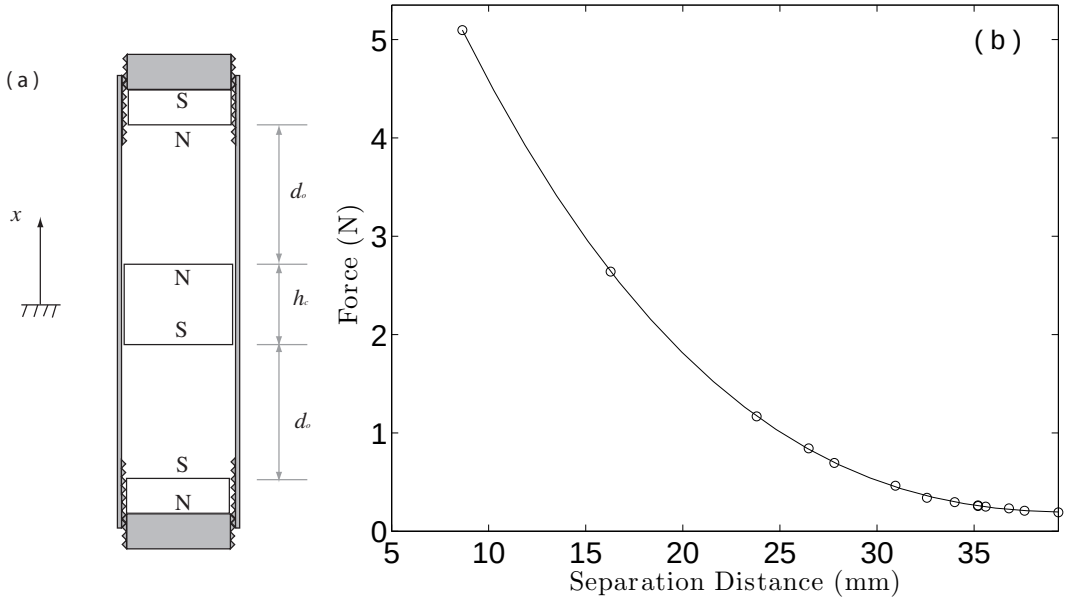

Fig. 1. A schematic diagram of the magnetic levitation system with threaded supports to position the outer magnets is shown in (a). Graph (b) shows the restoring force plotted as a function of the separation distance between the center and bottom magnet.

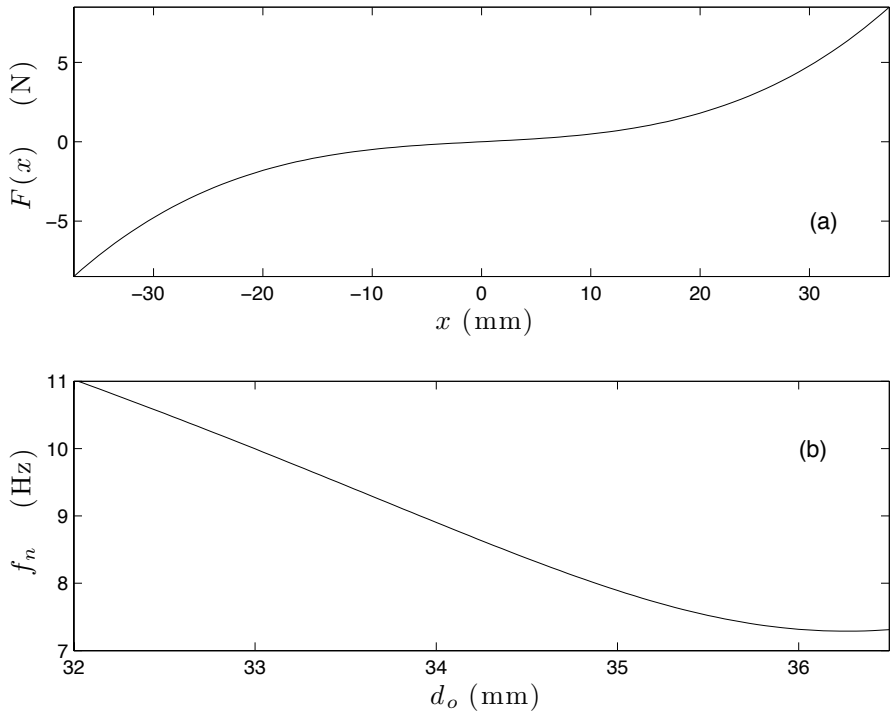

Fig. 2. Graph (a) shows the force-displacment relationship for $d_o = 37.3$ (mm) and the coefficients of Table 1. Graph (b) illustrates a change in the linear resonances as a function of the magnet spacing.

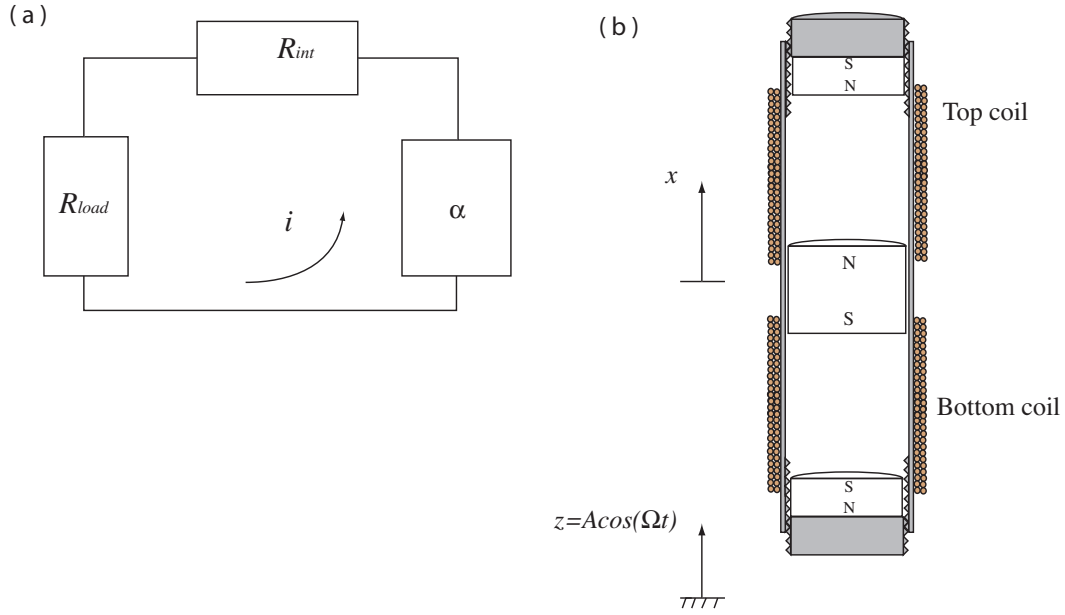

Fig. 3. Circuit diagram (a) for the energy harvesting device shown in (b).

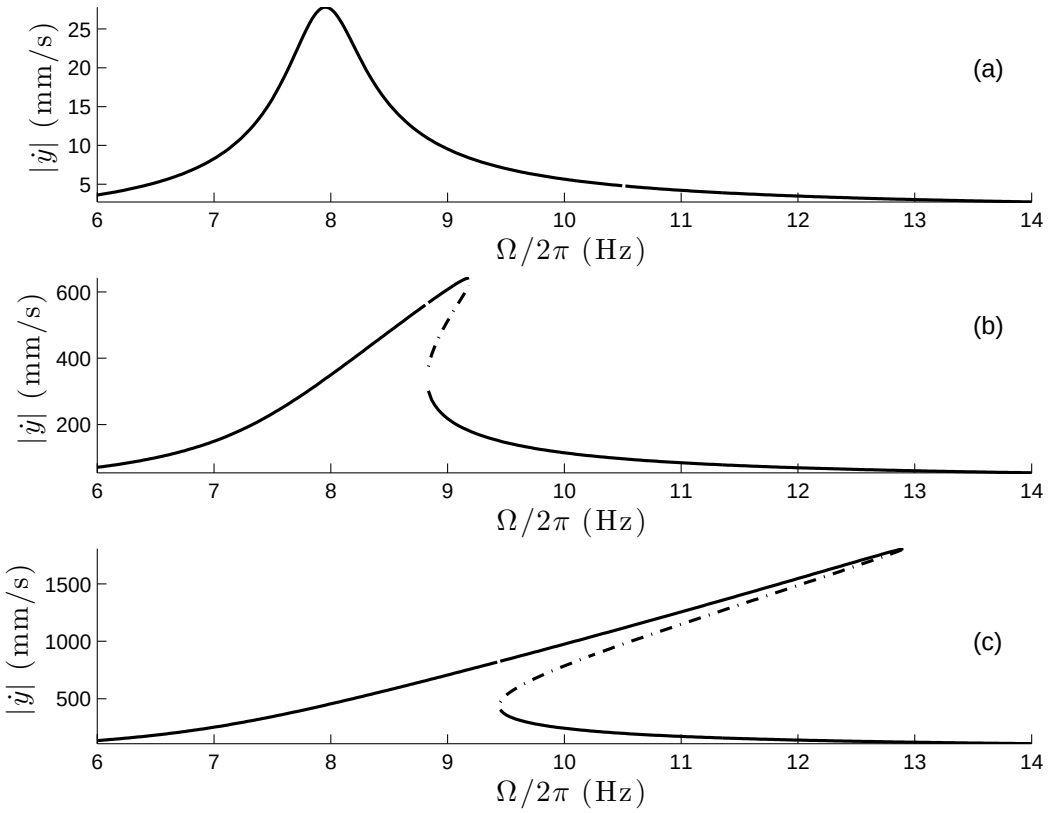

Fig. 4. Relative velocity response for different excitation amplitudes: (a) $F_1 = 0.1$ (m/s^2), (b) $F_1 = 2$ (m/s^2), and (c) $F_1 = 4$ (m/s^2). With the exception of the damping ratio, set to $\zeta = 0.05$, the experimentally identified parameters from Table 1 were used. Solid line denotes stable periodic solutions and a dashed line represents unstable periodic solutions.

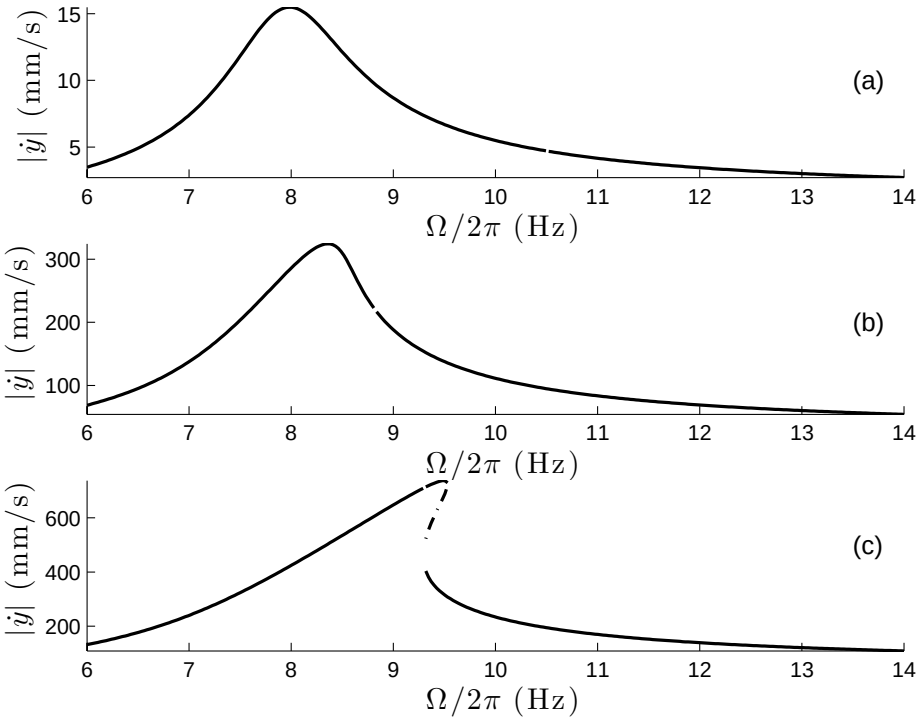

Fig. 5. Relative velocity response for different excitation amplitudes: (a) $F_1 = 0.1$ (m/s^2), (b) $F_1 = 2$ (m/s^2), and (c) $F_1 = 4$ (m/s^2). With the exception of the damping ratio, set to $\zeta = 0.09$, the experimentally identified parameters from Table 1 were used. Solid line denotes stable periodic solutions and a dashed line represents unstable periodic solutions.

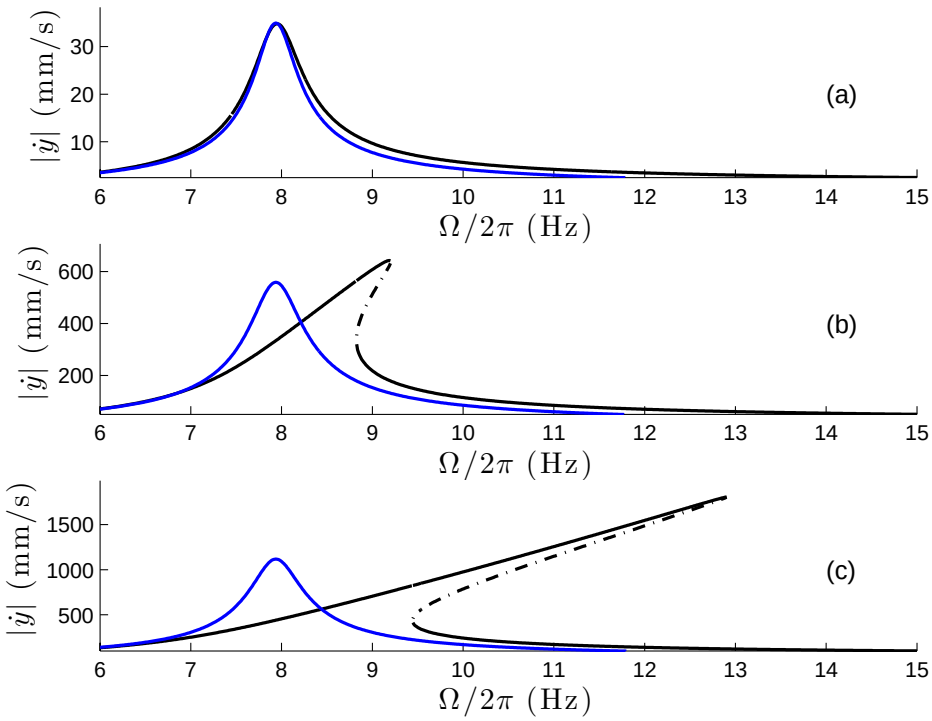

Fig. 6. Frequency response curves of the relative velocity for the magnetic levitation system and a linear oscillator with parameters $\gamma = 0.036$ and $\omega_n = 49.87$ (rad/s) which give matching peak responses for $F_1 = 0.1$ (m/s^2), graph (a). The remaining graphs are for relatively larger excitation amplitudes: (b) $F_1 = 2$ (m/s^2) and (c) $F_1 = 4$ (m/s^2). Solid line denotes stable periodic solutions and a dashed line represents unstable periodic solutions.

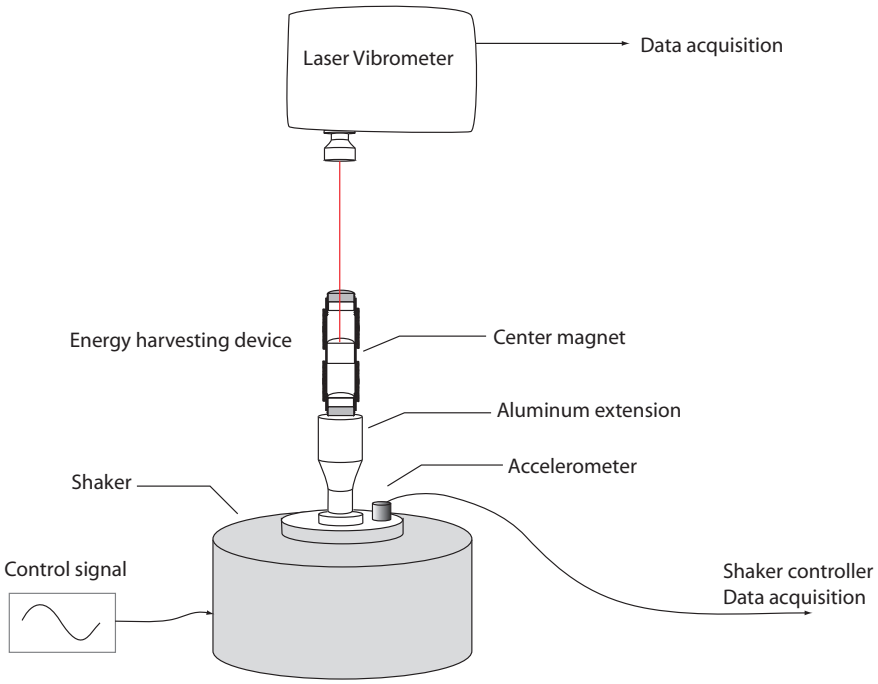

Fig. 7. Schematic diagram of the primary experimental instrumentation and shaker controller. A laser vibrometer was used to measure the absolute velocity of the center magnet during calibration. Afterwards, the center magnet velocity was determined from the measured coil voltage.

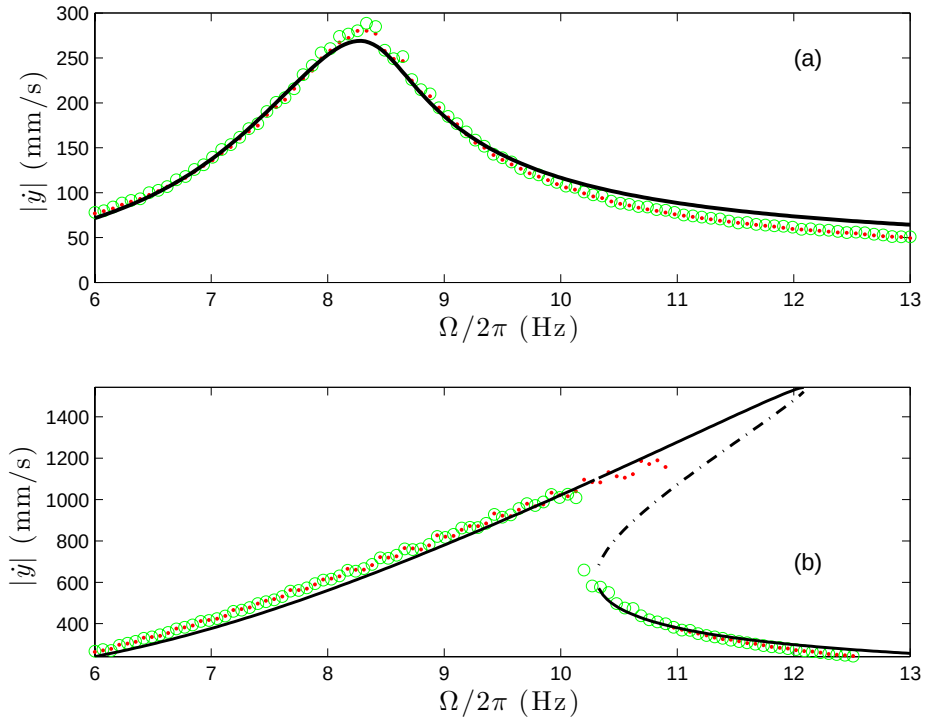

Fig. 8. Experimental velocity response amplitudes from forward (red dots) and reverse frequency sweeps (green circles) are compared with theory. Theoretical predictions are separated into stable solutions (solid black line) and unstable solutions (dashed black line). Graph (a) shows results for $F_1 = 2.1$ (m/s^2) and the results of graph (b) are for $F_1 = 8.4$ (m/s^2).

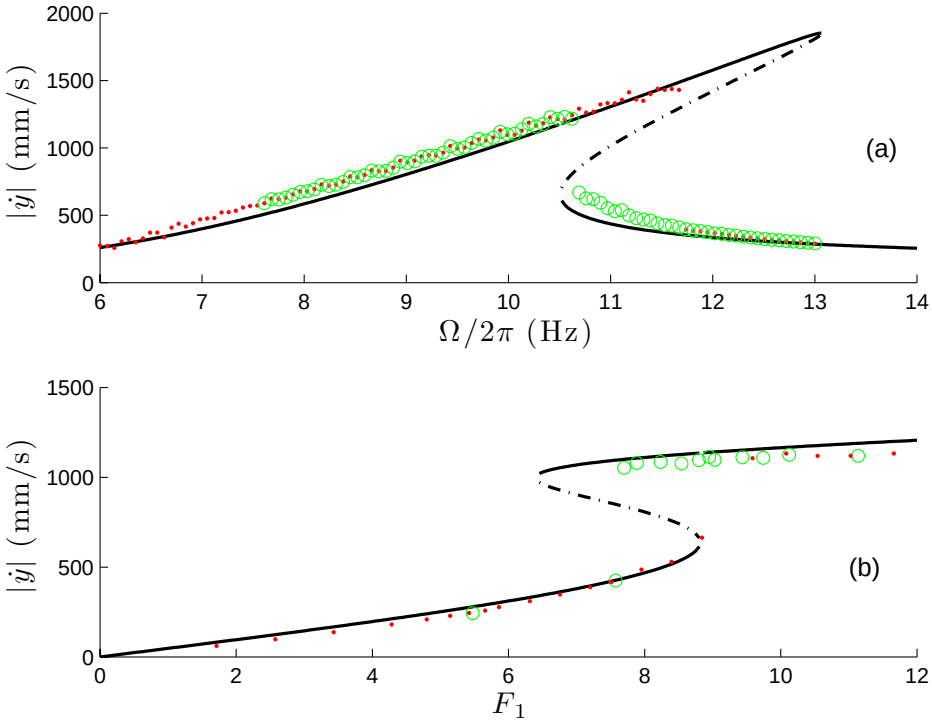

Fig. 9. Experimental velocity response amplitudes from forward (red dots) and reverse frequency sweeps (green circles) are compared in graph (a) for $F_1 = 9.3$ (m/s^2). Graph (b) shows velocity response amplitudes results from upward and downward input excitation amplitude sweeps for a constant frequency of $\Omega = 20.8\pi$ (rad/s). Theoretical predictions are separated into stable solutions (solid black line) and unstable solutions (dashed black line).